LETTER

Superfluorescence from lead halide perovskite quantum dot superlattices

Gabriele Rainò[1,2,3,5]*, Michael A. Becker[3,4,5], Maryna I. Bodnarchuk[2], Rainer F. Mahrt[3], Maksym V. Kovalenko[1,2]* & Thilo Stöferle[3]*

An ensemble of emitters can behave very differently from its individual constituents when they interact coherently via a common light field. After excitation of such an ensemble, collective coupling can give rise to a many-body quantum phenomenon that results in short, intense bursts of light—so-called superfluorescence[1]. Because this phenomenon requires a fine balance of interactions between the emitters and their decoupling from the environment, together with close identity of the individual emitters, superfluorescence has thus far been observed only in a limited number of systems, such as certain atomic and molecular gases and a few solid-state systems[2–7]. The generation of superfluorescent light in colloidal nanocrystals (which are bright photonic sources practically suited for optoelectronics[8,9]) has been precluded by inhomogeneous emission broadening, low oscillator strength, and fast exciton dephasing. Here we show that caesium lead halide (CsPbX$_3$, X = Cl, Br) perovskite nanocrystals[10–13] that are self-organized into highly ordered three-dimensional superlattices exhibit key signatures of superfluorescence. These are dynamically red-shifted emission with more than 20-fold accelerated radiative decay, extension of the first-order coherence time by more than a factor of four, photon bunching, and delayed emission pulses with Burnham–Chiao ringing behaviour[14] at high excitation density. These mesoscopically extended coherent states could be used to boost the performance of opto-electronic devices[15] and enable entangled multi-photon quantum light sources[16,17].

Spontaneous emission of photons—such as happens in the process of fluorescence that is commonly used in displays and lighting—occurs because of coupling between excited two-level systems (TLS) and the vacuum modes of the electromagnetic field, effectively stimulated by its zero-point fluctuations. In 1954, Dicke predicted[18] that an ensemble of N identical TLS confined in a volume smaller than about λ^3 (where λ is the corresponding emission wavelength of the TLS) can exhibit coherent and cooperative spontaneous emission. This so-called super-radiant emission results from the coherent coupling between individual TLS through the common vacuum modes, effectively leading to a single giant emitting dipole from all participating TLS. Superradiant emission has been observed in distinctly different physical systems, such as molecular aggregates and crystals[19], nitrogen vacancy centres in diamond[20] and epitaxially grown quantum dots[21] (QDs). In the case when the excited TLS are initially fully uncorrelated, the coherence can be established only through spontaneously triggered correlations due to quantum fluctuations rather than by coherent excitation. When this occurs, a so-called superfluorescence (SF) pulse is emitted[1] (Fig. 1, illustrated for the present study). Both superradiant emission and coherent SF bursts are characterized by an accelerated radiative decay time $\tau_{SF} \propto \tau_{SE}/N$, where the exponential decay time τ_{SE} of spontaneous emission from the uncoupled TLS is shortened by the number of coupled emitters N. In addition, SF exhibits the following fundamental signatures, the magnitudes of which are also dependent on the excitation density: (i) a delay or build-up time $\tau_D \propto \log(N)/N$ during which the emitters couple and phase-synchronize to each other, and which

corresponds to the time delay between the excitation and onset of the cooperative emission (Fig. 1); and (ii) coherent Rabi-type oscillations in the time domain due to the strong light–matter interaction, known as Burnham–Chiao ringing[14,22].

Superfluorescence was first observed in a dense gas of hydrogen fluoride[2], and then in a limited number of solid-state systems, such as CuCl nanocrystals (NCs) formed in a NaCl matrix[4], KCl crystals doped with peroxide anions[3] (O$_2^-$), and some select semiconductor crystals (ZnTe and InGaAs/GaAs multi-quantum wells)[5,6]. Practical implementation of such an enhanced radiative property is a persistent challenge. Besides stringent requirements for the emissive material (for example, high oscillator strength, small inhomogeneous line-broadening, small exciton dephasing), equally important are structural, optical and device engineerability. Colloidal semiconductor NCs, also known as colloidal QDs, could fill this gap as they are structurally and optically versatile, and highly suited for the entire visible spectral range. Although they are actively pursued for photonic applications[8,9,23], they have not been reported to exhibit SF.

Here we use colloidal NCs of caesium lead halide perovskites (CsPbX$_3$, X = Cl, Br) that can be synthesized with narrow size dispersion and are known to exhibit moderate quantum confinement effects, resulting in narrow-band emission combined with exceptionally large oscillator strength from a bright triplet state[10,11,24]. In order to foster cooperative behaviour, we employ structurally well-defined, long-range-ordered, and densely packed arrays of such NCs, known as superlattices, produced by means of solvent-drying-induced spontaneous assembly[25–28]. Similarly, regular arrays of II–VI semiconductor NCs have been used to obtain collective effects in the electronic domain, that is, band-like transport[15]. Figure 2a outlines superlattice formation (see also Methods), using a solution of highly monodispersed CsPbBr$_3$ NCs with a mean size of 9.5 nm and size standard deviation of less
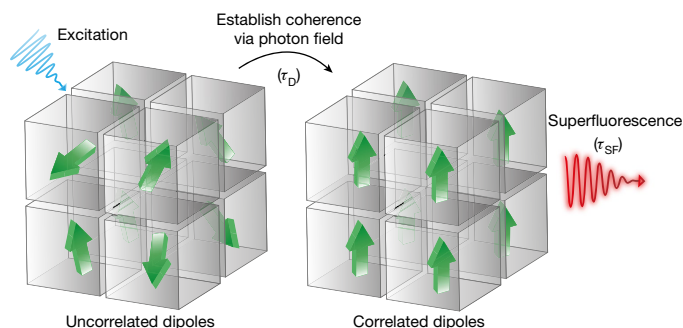

Fig. 1 | Schematic of the build-up process of SF. An initially uncorrelated ensemble of TLS (randomly oriented green arrows) is excited by a light pulse (blue arrow, top left). After time τ_D their phases are synchronized (aligned green arrows) such that they cooperatively emit a SF light pulse (red arrow at right) with a characteristic decay time τ_{SF}. Grey cubes represent long-range-ordered self-assembled superlattices.

[1]Department of Chemistry and Applied Bioscience, Institute of Inorganic Chemistry, ETH Zurich, Zurich, Switzerland. [2]Laboratory of Thin Films and Photovoltaics, Empa — Swiss Federal Laboratories for Materials Science and Technology, Dübendorf, Switzerland. [3]IBM Research — Zurich, Rüschlikon, Switzerland. [4]Optical Materials Engineering Laboratory, ETH Zurich, Zurich, Switzerland. [5]These authors contributed equally: G. Rainò; M. A. Becker. *e-mail: rainog@ethz.ch; mvkovalenko@ethz.ch; tof@zurich.ibm.com
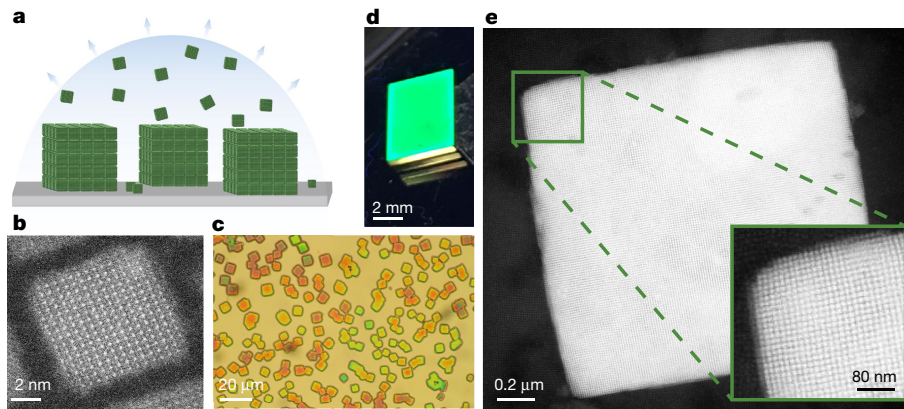
Fig. 2 | Formation of CsPbX$_3$ (X = Cl, Br) NC superlattices by drying-mediated self-assembly. a, Illustration of the assembly process: a controlled evaporation (indicated by the pale blue arrows) of the solvent leads to the formation of micrometre-size cuboidal superlattices. **b**, High-resolution image (obtained using high-angle annular dark-field scanning transmission electron microscopy, HAADF–STEM) of a single CsPbBr$_3$ NC. **c**, Optical microscope image and **d**, photograph (under ultraviolet light) of a layer of micrometre-sized, three-dimensional, cuboidal-shaped NC superlattices. **e**, HAADF–STEM image of a single superlattice of CsPbBr$_3$ NCs. The cubic shape of the individual perovskite NC building blocks is translated into the symmetry of the superlattice (simple cubic packing). Inset, magnified view of the boxed area, showing the individual NCs.

than 5% (Extended Data Fig. 1). In the self-assembly process, cuboidal individual superlattice domains are formed (that is, supercrystals), each consisting of up to several million NCs. Optical microscopy (Fig. 2c) reveals superlattices with a lateral size of up to 5 μm, randomly distributed in a uniform film on a 5 mm × 7 mm sample (Fig. 2d). Transmission electron microscopy confirms that highly ordered super-lattices consist of well-separated individual NCs (Fig. 2e and Extended Data Fig. 2). More details of the self-assembly process are reported in the Methods section.

Figure 3a displays the photoluminescence (PL) spectrum of a single CsPbBr$_3$ superlattice (excited at 3.06 eV) exhibiting two emission peaks. This and all other optical measurements were performed at a temperature of 6 K in vacuum or in a helium atmosphere (see Methods for details). The high-energy emission peak coincides with the centre energy of PL from a disordered dense film of CsPbBr$_3$ NCs (in a glassy state) and is therefore assigned to uncoupled QDs. In addition, a narrow, red-shifted emission peak appears in PL from superlattices, which we assign to the emission of coupled QDs, which is best fitted with a Lorentzian (full-width at half-maximum, FWHM$_{coupled}$ = 11 meV). The peaks from the uncoupled QDs in a superlattice and in the glassy films are best fitted with a Gaussian, as expected for disordered ensembles. The width of the uncoupled QD emission (FWHM$_{uncoupled}$ = 55 meV) is slightly broader than that of the amorphous film (FWHM$_{amorphous}$ = 35 meV), which can be explained by assuming that more 'identical QDs' within the superlattice are now forming the peak from coupled QDs while the remaining uncoupled ones appear more disordered than the inhomogeneous energy distribution of the primary QD material. We can exclude the possibility that the red-shifted feature, which is about 70 meV lower in energy than the uncoupled QD emission, originates from emission from trions, bi-excitons or multi-excitons because the energy shifts of these last three species are reportedly[11,12] 10−20 meV, and these would also be observable in the disordered ensemble. The number and interaction strength of coupled QDs determine the magnitude of the energy shift. Statistics from 10 superlattices from different samples give an average static red-shift of (64 ± 6) meV, average FWHM$_{coupled}$ = (15 ± 4) meV and average FWHM$_{uncoupled}$ = (49 ± 21) meV. In most superlattices, we observe a substructure in this red-shifted emission band, which we attribute to the presence of several slightly different independent domains within the same individual superlattice.

A central feature of cooperative emission is the modification of the radiative lifetime[18], as demonstrated experimentally in several quantum emitters[6,20,21]. In time-resolved PL decay measurements at a very low excitation fluence (5 nJ cm^{-2}), we do not observe a significant
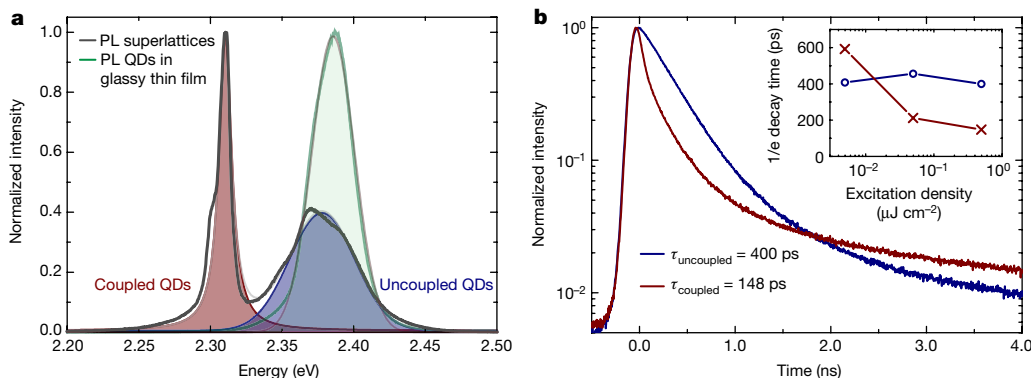

Fig. 3 | Optical properties of CsPbBr$_3$ QD superlattices. a, PL spectrum of a single CsPbBr$_3$ superlattice (black solid line). The high-energy band is assigned to the emission of uncoupled QDs. The low-energy band is the result of the emission of coupled QDs and is not present in glassy films of NCs (green solid line). The shaded areas are fits to the data (see main text). **b**, Time-resolved PL decay of the two emission bands at 500 nJ cm^{-2} excitation fluence after applying suitable spectral filters to separate the two components (blue curve, from uncoupled QDs; dark-red curve, from coupled QDs). The 1/e-decay time of the two bands ($\tau_{coupled}$ and $\tau_{uncoupled}$, respectively) are also indicated. With increasing excitation fluence, the decay from the coherently coupled QDs is substantially faster than from the uncoupled ones. Inset, power-dependence of the 1/e-decay times of both components.

modification of the decay of the coupled QD emission compared to that of the uncoupled QD emission (Fig. 3b inset). The absence of accelerated emission at vanishing excitation fluence and the presence of the red-shifted feature in PL excitation scans (Extended Data Fig. 3) corroborate that the static red-shift of ~70 meV originates from incoherent coupling of the QDs in the ground state, similar to that found in various molecular aggregates[19]. At a slightly higher excitation fluence (500 nJ cm^{-2} per pulse), we already observe an accelerated PL decay of the coupled QD emission peak in comparison to the PL decay of uncoupled QDs, with 1/e decay times of $\tau_{SF} = 148$ ps and $\tau_{QD} = 400$ ps, respectively (Fig. 3b). In contrast to the predominantly mono-exponential decay of the uncoupled QDs, this SF emission decay is well approximated by a stretched exponential[29] (see Methods section), because the number of excited coupled emitters, and therefore the emission acceleration, varies during the decay. Furthermore, in contrast to the uncoupled QDs, the SF decay time is strongly dependent on excitation power (Fig. 3b inset): this is because it scales with the coupling strength among the QDs, which is given by the intensity of the common light-field that effectively corresponds to a change in the number of coherently coupled QDs. When the spectrally and temporally integrated emission is fitted with a power law, we obtain an exponent of 1 (Extended Data Fig. 4), indicating that excitation-density-dependent non-radiative decay channels (for example, Auger recombination) are absent. Notably, no threshold behaviour as occurs for amplified spontaneous emission is observed.

The cooperative emission process strongly influences the coherence of the emitted light. First-order correlation measurements of each of the two emission peaks by means of a Michelson interferometer allow us to monitor the interference pattern and therefore the phase coherence time (Fig. 4a). The emission band of the uncoupled QDs exhibits a coherence time of 38 fs, best fitted with a Gaussian decay (Fig. 4a, upper graph), typical of incoherent (thermal) light sources. The emission from the coherently coupled QDs (Fig. 4a, lower graph) exhibits a much longer coherence time with an exponential decay of 140 fs. For some superlattices, a Gaussian decay is observed (Extended Data Fig. 5a), which might be attributed to number fluctuations within the coherent SF state[30].

Second-order coherence of the emitted light is evinced by the statistics of the photon arrival time on a detector[31]. Typical coherent light, as from a laser, shows a random (Poissonian) distribution of photon arrival times, whereas a single TLS exhibits photon antibunching (a sub-Poissonian distribution). In contrast, the cooperative emission from coupled QDs leads to coherent multi-photon emission bursts. Figure 4b reports the second-order correlation function, $g^{(2)}(\tau) = \langle I(t)I(t+\tau)\rangle/\langle I(t)\rangle^2$, for both PL emission bands, where $I(t)$ is the signal intensity at time t and $\langle I(t)\rangle$ is its statistical average. For the uncoupled QD emission (Fig. 4b, upper graph), the plot is flat ($g^{(2)}(\tau) = 1$) because the experimental temporal resolution (40 ps) is insufficient to resolve the expected thermal bunching. The SF emission band, however, shows pronounced photon bunching (Fig. 4b, lower graph) because the coherent coupling leads to the correlated emission of multiple photons within a short time interval. Photon bunching is only observable in superlattices with one or a few SF domains (that is, where no substructure is visible in the red-shifted emission band) because spectrally overlapping uncorrelated aggregated domains within the same superlattice reduce the bunching peak's visibility, as predicted by theory[32]. Yet it is a robust effect that is observed with pulsed excitation and also for mixed-halide (CsPbBr$_2$Cl, emitting at higher energies) QD superlattices (see Extended Data Figs. 5b and 6b, respectively). Remarkably, some superlattices with supposedly well-isolated coherently coupled QDs exhibit $g^{(2)}(0) > 2$ (Fig. 4 inset), similarly to superthermal emission[31]. The exponential decay time of the second-order correlation is of the order of the radiative decay time of the SF emission for low excitation densities ($\tau_{g^{(2)}} = 224$ ps).

SF emission exhibits very distinct characteristics in the time domain under strong driving conditions. Figure 5a shows a streak camera image acquired at an excitation fluence of 600 μJ cm^{-2}, where a finite
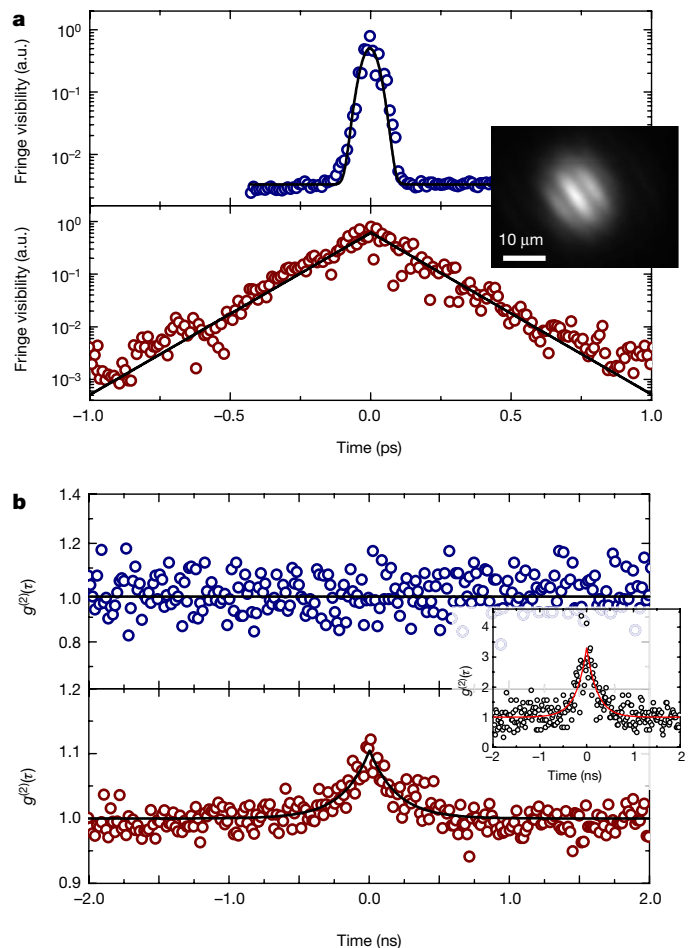

Fig. 4 | First- and second-order coherence properties of CsPbBr$_3$ QD superlattices. a, First-order correlation of the two emission bands as obtained from the interference fringe visibility using a Michelson interferometer. The high-energy band of the uncoupled QDs has a very short phase coherence time (<40 fs, upper graph, blue symbols), whereas the red-shifted band from the coupled QDs is characterized by much longer phase coherence (140 fs, lower graph, dark-red symbols). The solid lines are fits to the data (see main text). a.u., arbitrary units. Inset, an example of the real-space interferogram. **b**, Second-order correlation function, $g^{(2)}(\tau)$, obtained with a Hanbury–Brown and Twiss set-up in start–stop configuration. For the high-energy band (upper graph, blue symbols), a flat profile with $g^{(2)}(\tau) = 1$ is observed. The red-shifted emission band (lower graph, dark-red symbols) from the SF emission displays a pronounced bunching peak, characteristic of the correlated emission during a photon burst. The data are fitted to the function $g^{(2)}(\tau) = 1 + A\exp(-|\tau|/\tau_c)$ (solid lines), where A is an amplitude prefactor, and τ_c the characteristic decay time of the second order coherence. Inset, an example of superbunching with $g^{(2)}(0) > 2$ from a single superlattice. Black open circles are experimental data while the red curve represents the best fit to the function described above.

rise time and subsequent oscillation of the emission are observed in addition to a much shortened radiative decay. Quantitative analysis of spectrally integrated PL decay traces for various excitation power densities is shown in Fig. 5b (for details see Methods). As excitation fluence is increased, the decay time shortens to 14 ps (Fig. 5c, upper panel). From this shortening, which is an order of magnitude stronger than that reported for the collective emission from other QD systems[4,21], we can estimate the average number of coherently coupled QDs to be $N \approx 28$. This is only an effective value and is a conservative estimate, because the energetic disorder of the QD emission energies (FWHM$_{coupled} = 11$ meV) still substantially exceeds the emission peak width of individual QDs (typically[11] FWHM ≈ 1 meV) and thereby effectively reduces the coherent coupling[33]. The SF emission undergoes
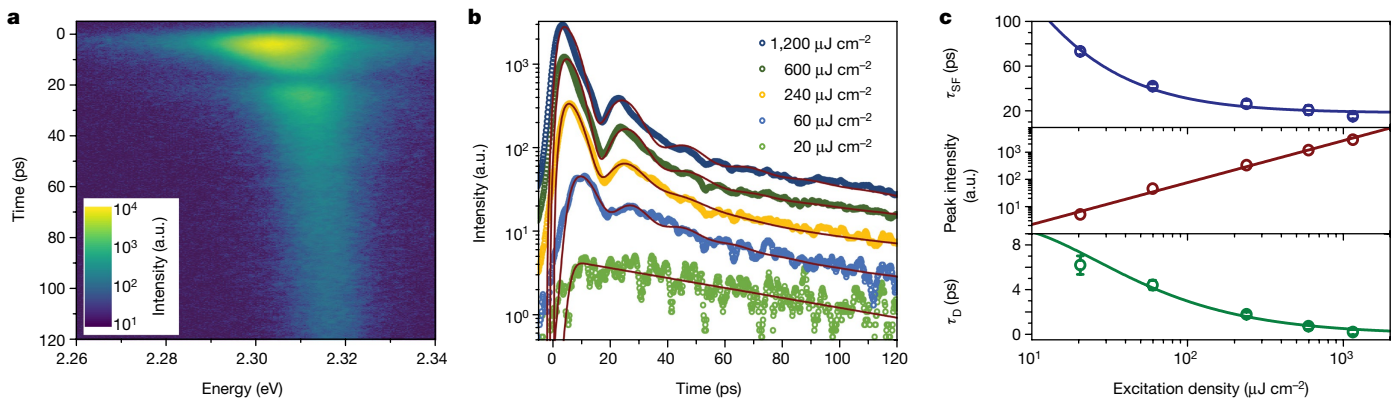
Fig. 5 | Burnham–Chiao ringing behaviour of CsPbBr$_3$ QD superlattices. a, Streak camera image of SF dynamics obtained with a high excitation density of 600 μJ cm^{-2}. See Methods for details. **b**, Extracted time-resolved emission intensity traces for five different excitation powers (see key). Solid red lines are weighted best-fits to a model that employs a bi-exponential decay function with damped oscillations. **c**, Top, effective SF decay (τ_{SF}, blue circles) as a function of the excitation power density fitted according to the SF model (solid blue line). Middle, dark-red circles represent the peak SF emission intensity that increases superlinearly with excitation power, corresponding to a power-law dependence with an exponent $\alpha = 1.5 \pm 0.1$ (solid dark-red line). Bottom, the extracted delay time τ_D (green circles) decreases at high excitation power due to the increased interaction among the emitters. The green solid line is the best fit according the model described in the Methods section. The error bars represent the parameters' fit uncertainty.

a dynamical red-shift of up to 15 meV owing to renormalization of the emission energy from the coherent coupling[7], which decreases in the course of the decay as the number of excited dipoles reduces (Extended Data Fig. 7). The peak intensity increases superlinearly over three orders of magnitude (Fig. 5c, middle panel) according to a power-law dependence with an exponent of $\alpha = 1.5 \pm 0.1$, deviating from the theoretically expected[7] value of $\alpha = 2$, presumably owing to saturation effects[5]. Nevertheless, no substantial quenching of the emission for high excitation fluences was found, verifying that the decay remains essentially radiative (Extended Data Fig. 4d). Furthermore, a shortening of the SF build-up time (τ_D), after which the photon burst is emitted, is observed (Fig. 5c, bottom panel). This characteristic of SF is a consequence of the time it takes for the individual dipoles to become phase-locked and scales with the number N of excited coupled QDs according to $\tau_D \propto \log(N)/N$ (see Methods section).

As SF crucially depends on low decoherence and low inhomogeneous energy variation, it should be noted that SF coupling is strongly affected by the environment around the QDs (for example, the number of free ligands, which are the molecules used to passivate the NC surface), by the superlattice assembly, and by the quality of the QDs themselves. Thus, while a large fraction of the superlattices display the red-shifted emission from coupled QDs, the amount of photon-bunching and Burnham–Chiao ringing varied from superlattice to superlattice. However, experiments employing different batches of NCs and super-lattice assemblies of CsPbBr$_3$ and CsPbBr$_2$Cl NCs (see Extended Data Figs. 6–9) were consistently reproducible, but further optimization of the synthesis and assembly is likely to improve the yield of SF domains. It is important to note that experiments on control samples with diluted, uncoupled QDs under similar excitation conditions do not show any of the above-mentioned signatures of SF (Extended Data Fig. 10), proving that the observed peculiar emission characteristics of QD superlattices arise from a genuine multi-particle effect.

Our measurements reveal that coherent SF coupling can be achieved in long-range-ordered self-assembled superlattices of fully inorganic CsPbX$_3$ perovskite NCs, resulting in strong emission bursts. Colloidal NCs and their assemblies have proven to be excellent building blocks for a large variety of opto-electronic devices, and these cooperative effects now allow modification of the opto-electronic properties beyond what is possible at the individual QD level with chemical engineering approaches. This opens up new opportunities for high-brightness and multi-photon quantum light sources, and could enable the exploitation of cooperative effects for long-range quantum transport and ultra-narrow tunable lasers.

Online content

Any methods, additional references, Nature Research reporting summaries, source data, statements of data availability and associated accession codes are available at https://doi.org/10.1038/s41586-018-0683-0.

1. Bonifacio, R. & Lugiato, L. A. Cooperative radiation processes in two-level systems: superfluorescence. *Phys. Rev. A* **11**, 1507–1521 (1975).
2. Skribanowitz, N., Herman, I. P., MacGillivray, J. C. & Feld, M. S. Observation of Dicke superradiance in optically pumped HF gas. *Phys. Rev. Lett.* **30**, 309–312 (1973).
3. Malcuit, M. S., Maki, J. J., Simkin, D. J. & Boyd, R. W. Transition from superfluorescence to amplified spontaneous emission. *Phys. Rev. Lett.* **59**, 1189–1192 (1987).
4. Miyajima, K., Kagotani, Y., Saito, S., Ashida, M. & Itoh, T. Superfluorescent pulsed emission from biexcitons in an ensemble of semiconductor quantum dots. *J. Phys. Condens. Matter* **21**, 195802 (2009).
5. Dai, D. C. & Monkman, A. P. Observation of superfluorescence from a quantum ensemble of coherent excitons in a ZnTe crystal: evidence for spontaneous Bose-Einstein condensation of excitons. *Phys. Rev. B* **84**, 115206 (2011).
6. Noe, G. T. II et al. Giant superfluorescent bursts from a semiconductor magneto-plasma. *Nat. Phys.* **8**, 219–224 (2012).
7. Cong, K. et al. Dicke superradiance in solids. *J. Opt. Soc. Am. B* **33**, C80–C101 (2016).
8. Talapin, D. V., Lee, J.-S., Kovalenko, M. V. & Shevchenko, E. V. Prospects of colloidal nanocrystals for electronic and optoelectronic applications. *Chem. Rev.* **110**, 389–458 (2010).
9. Kovalenko, M. V. et al. Prospects of nanoscience with nanocrystals. *ACS Nano* **9**, 1012–1057 (2015).
10. Protesescu, L. et al. Nanocrystals of cesium lead halide perovskites (CsPbX$_3$, X=Cl, Br, and I): novel optoelectronic materials showing bright emission with wide color gamut. *Nano Lett.* **15**, 3692–3696 (2015).
11. Rainò, G. et al. Single cesium lead halide perovskite nanocrystals at low temperature: fast single-photon emission, reduced blinking, and exciton fine structure. *ACS Nano* **10**, 2485–2490 (2016).
12. Fu, M. et al. Neutral and charged exciton fine structure in single lead halide perovskite nanocrystals revealed by magneto-optical spectroscopy. *Nano Lett.* **17**, 2895–2901 (2017).
13. Kovalenko, M. V., Protesescu, L. & Bodnarchuk, M. I. Properties and potential optoelectronic applications of lead halide perovskite nanocrystals. *Science* **358**, 745–750 (2017).
14. Burnham, D. C. & Chiao, R. Y. Coherent resonance fluorescence excited by short light pulses. *Phys. Rev.* **188**, 667–675 (1969).
15. Kagan, C. R. & Murray, C. B. Charge transport in strongly coupled quantum dot solids. *Nat. Nanotechnol.* **10**, 1013–1026 (2015).
16. Afek, I., Ambar, O. & Silberberg, Y. High-NOON states by mixing quantum and classical light. *Science* **328**, 879–881 (2010).
17. Muñoz, C. S. et al. Emitters of N-photon bundles. *Nat. Photon.* **8**, 550–555 (2014).
18. Dicke, R. H. Coherence in spontaneous radiation processes. *Phys. Rev.* **93**, 99–110 (1954).
19. Spano, F. C. The spectral signatures of Frenkel polarons in H- and J-aggregates. *Acc. Chem. Res.* **43**, 429–439 (2010).

20. Bradac, C. et al. Room-temperature spontaneous superradiance from single diamond nanocrystals. *Nat. Commun.* **8**, 1205 (2017).
21. Scheibner, M. et al. Superradiance of quantum dots. *Nat. Phys.* **3**, 106–110 (2007).
22. Heinzen, D. J., Thomas, J. E. & Feld, M. S. Coherent ringing in superfluorescence. *Phys. Rev. Lett.* **54**, 677–680 (1985).
23. Shirasaki, Y., Supran, G. J., Bawendi, M. G. & Bulović, V. Emergence of colloidal quantum-dot light-emitting technologies. *Nat. Photon.* **7**, 13–23 (2013).
24. Becker, M. A. et al. Bright triplet excitons in caesium lead halide perovskites. *Nature* **553**, 189–193 (2018).
25. Boles, M. A., Engel, M. & Talapin, D. V. Self-assembly of colloidal nanocrystals: from intricate structures to functional materials. *Chem. Rev.* **116**, 11220–11289 (2016).
26. Murray, C. B., Kagan, C. R. & Bawendi, M. G. Synthesis and characterization of monodisperse nanocrystals and close-packed nanocrystal assemblies. *Annu. Rev. Mater. Sci.* **30**, 545–610 (2000).
27. Geuchies, J. J. et al. In situ study of the formation mechanism of two-dimensional superlattices from PbSe nanocrystals. *Nat. Mater.* **15**, 1248–1254 (2016).
28. Nagaoka, Y. et al. Nanocube superlattices of cesium lead bromide perovskites and pressure-induced phase transformations at atomic and mesoscale levels. *Adv. Mater.* **29**, 1606666 (2017).
29. Temnov, V. V. & Woggon, U. Superradiance and subradiance in an inhomogeneously broadened ensemble of two-level systems coupled to a low-Q cavity. *Phys. Rev. Lett.* **95**, 243602 (2005).
30. Whittaker, D. M. & Eastham, P. R. Coherence properties of the microcavity polariton condensate. *Europhys. Lett.* **87**, 27002 (2009).
31. Jahnke, F. et al. Giant photon bunching, superradiant pulse emission and excitation trapping in quantum-dot nanolasers. *Nat. Commun.* **7**, 11540 (2016).
32. Temnov, V. V. & Woggon, U. Photon statistics in the cooperative spontaneous emission. *Opt. Express* **17**, 5774 (2009).
33. Ishikawa, A., Miyajima, K., Ashida, M., Itoh, T. & Ishihara, H. Theory of superfluorescence in highly inhomogeneous quantum systems. *J. Phys. Soc. Jpn.* **85**, 034703 (2016).

Author contributions The work originated from continuing interactions between G.R., M.V.K., R.F.M. and T.S. M.I.B. prepared the samples and performed their structural characterization. G.R., M.A.B. and T.S. performed the optical experiments, and interpreted the data with input from R.F.M. G.R. and M.A.B. wrote the manuscript with input from all the co-authors. R.F.M., M.V.K. and T.S. supervised the work.

Competing interests The authors declare no competing interests.

Additional information
Extended data is available for this paper at https://doi.org/10.1038/s41586-018-0683-0.
Reprints and permissions information is available at http://www.nature.com/reprints.
Correspondence and requests for materials should be addressed to G.R., M.V.K. and T.S.
Publisher's note: Springer Nature remains neutral with regard to jurisdictional claims in published maps and institutional affiliations.

METHODS

Synthesis of CsPbBr₃ nanocrystals. In a 25 ml three-necked flask, PbBr$_2$ (69 mg, 0.188 mmol, Aldrich, 99%) was suspended in octadecene (5 ml), dried at 100 °C for 30 min, and mixed with oleic acid (0.5 ml, vacuum-dried at 100 °C) and oleylamine (0.5 ml vacuum-dried at 100 °C). When the PbBr$_2$ had dissolved, the reaction mixture was heated up to 180 °C and preheated caesium oleate in octadecene (0.4 ml, 0.125 M) was injected. The reaction mixture was cooled immediately with an ice bath to room temperature.

Synthesis of CsPbBr₂Cl nanocrystals. In a 25 ml three-necked flask, PbBr$_2$ (45 mg, 0.12 mmol, Aldrich, 99%), PbCl$_2$ (18 mg, 0.064 mmol, ABCR) and 1 ml trioctylphosphine (Strem, 97%) was suspended in octadecene (5 ml), dried at 100 °C for 30 min, and mixed with oleic acid (0.5 ml, vacuum-dried at 100 °C) and oleylamine (0.5 ml vacuum-dried at 100 °C). When the PbCl$_2$ and PbBr$_2$ had dissolved, the reaction mixture was heated up to 180 °C and preheated caesium oleate in octadecene (0.4 ml, 0.125 M) was injected. The reaction mixture was cooled immediately with an ice bath to room temperature.

Purification and size-selection of CsPbX₃ (X = Cl, Br) nanocrystals. A critical factor for self-assembly of cubic-shaped CsPbX$_3$ NCs is to start with an initially high level of monodispersity. The crude solution was centrifuged at 12,100 revolutions per minute for 5 min, following which the supernatant was discarded, and the precipitate was dissolved in 300 μl hexane. The hexane solution was centrifuged again and the precipitate was discarded. The supernatant was diluted twice and used for further purification. Subsequently, two methods of purification of the NCs were applied: (a) 50 μl hexane, 0.6 μl oleic acid and 0.6 μl oleylamine were added to 50 μl NCs in hexane. The colloid was destabilized by adding 50 μl acetone, followed by centrifuging and dispersing the NCs in 300 μl toluene. This solution was used further for the preparation of the 3D superlattices. (b) 50 μl hexane and 100 μl toluene were added to 50 μl NCs in hexane. The colloid was destabilized by adding 50 μl acetonitrile, followed by centrifuging and dispersing the NCs in 300 μl toluene. This solution was used further for the preparation of the 3D superlattices.

Preparation of 3D superlattices. CsPbX$_3$ NC superlattices were prepared on glass or on 5 mm × 7 mm silicon substrates. Shortly before the self-assembly process, the silicon substrate was dipped into 4% solution of HF in water for 1 min, followed by washing with water. In a typical assembly process, the substrate was placed in a 10 mm × 10 mm × 10 mm Teflon well and 10 μl of purified NCs in toluene were spread onto the substrate. The well was covered with a glass slide and the toluene was then allowed to evaporate slowly. 3D superlattices of CsPbBr$_3$ NCs were formed upon complete evaporation of the toluene. Typical lateral dimensions of individual superlattices ranged from 1 μm to 10 μm, wherein some of them are arranged into clusters of several superlattices and others remain spatially well-isolated so that PL measurements can be performed on an individual superlattice. Greater purification or greater polydispersity of NCs led to disordered or 2D assemblies (glassy films). Furthermore, the formation of NC superlattices can serve to further narrow the size distribution and shape uniformity within the ensemble (with smaller or larger NCs being repelled from the NC domain), especially in the case of simple cubic packing of cubes, which is particularly intolerant of size and shape variations.

Optical spectroscopy. All measurements were performed at cryogenic temperatures (6 K). For PL, time-resolved PL, and second-order photon-correlation measurements on single superlattices, the sample was mounted in an evacuated liquid-helium flow cryostat on an *xyz* positioning stage and excited with a fibre-coupled excitation laser at an energy of 3.06 eV, either in continuous wave mode or pulsed mode with a 40 MHz repetition rate (pulse duration 50 ps). The excitation laser output was filtered with a short-pass filter and directed towards the long-working-distance 100× microscope objective (numerical aperture NA = 0.7) by a dichroic beam splitter, resulting in a nearly Gaussian-shaped excitation spot with a $1/e^2$ radius of 1.4 μm. The emission was collected via the same microscope objective and filtered using a tunable bandpass filter. For PL measurements, the collected light was then dispersed by a 300 lines per mm grating inside a 750 mm monochromator and detected by an EMCCD camera. For measurements of the PL decay, we filtered the emission with a tunable band-pass (FWHM = 15 nm) and recorded the decay with an avalanche photodiode single-photon detector with a time resolution of 30 ps connected to a time-correlated single-photon-counting system. The photon correlation was recorded using a similar set-up with two detectors in a Hanbury–Brown and Twiss configuration.

To record streak camera images and first-order coherence measurements, we excited the sample, which was mounted in an exchange-gas cryostat at 6 K, with a frequency-doubled regenerative amplifier seeded with a mode-locked Ti:sapphire laser with a pulse duration of 100–200 fs and a repetition rate of 1 kHz at 3.1 eV. For both excitation and detection, we used an 80 mm lens (NA = 0.013 after iris), resulting in an oval excitation spot area of 20 μm × 40 μm. The recorded PL was dispersed by a grating with 150 lines per mm in a 300 mm spectrograph and detected with a streak camera with a nominal time resolution of 2 ps and an instrument response function FWHM of 4 ps (see Extended Data Fig. 10). First-order

coherence measurements were performed using a Michelson interferometer. Here a non-polarizing beam splitter is used to split and recombine the light in the two interferometer arms, with one arm including a retroreflector on a delay stage with 100 nm step resolution. A tunable band-pass filter is applied to select the emission from either the coupled or the uncoupled QDs. The interferogram was recorded as real-space images of the recombined and focused detection beams on camera.

Optical properties of superfluorescence, superradiance and subradiance. As shown in Fig. 3b, we observed that the PL decay of the SF state is initially very fast and cannot be described with a single exponential because the decay rate Γ is dependent on the number of excited TLS, $\Gamma(N) \propto N$, and therefore decreases during the decay. Consequently, the SF decay rate should converge towards the decay rate of the uncoupled nanocrystals. However, we observe that the SF decay trace crosses the bi-exponential PL decay of the uncoupled QDs after 97% of the photons are emitted due to long decay components. These long decay components might originate from coupled QDs where the individual dipoles are out of phase and interfere destructively, a phenomenon known as subradiance[29,34]. In ensembles with inhomogeneously broadened PL, SF and subradiant states can coexist, and we find good agreement of the predicted excited state population with the measured PL decay[35].

An out-of-phase coupling amongst the QDs is expected to result in a higher photon energy of the subradiant state compared to the SF state. In Extended Data Figs. 7 and 9, we provide an analysis of the dynamical energy shift observed at high excitation power density for CsPbBr$_3$ and CsPbBr$_2$Cl QD superlattices, respectively. Examples of emission spectra at different times are reported in Extended Data Figs. 7a and 9a for the respective QD halide compositions. In Extended Data Figs. 7b and 9b, we plot the fitted centre photon energy of time-sliced PL spectra (2 ps bin) as a function of the fitted peak area (that is, the time-dependent emission intensity), as obtained from excitation-power-dependent streak camera images, again for both CsPbBr$_3$ and CsPbBr$_2$Cl QD superlattices. This effectively shows the energetic shift of the SF state as a function of its occupation, with the different curves representing different initial excitation powers. The green arrows indicate the time sequence of the individual analysed spectral traces. By increasing the excitation power, we observe that the initial dynamical red-shift is largest for the highest excitation power, as is expected from its relationship to the number of excited coupled QDs. Hence, when the number of excited coupled QDs decreases during the decay process, the emission energy blue-shifts to higher energy, as can be seen in Extended Data Figs. 7c and 9c where the fitted centre photon energy is plotted as a function of time. We observe the most pronounced energetic blue-shift for the highest excitation power, resulting in a final emission with a photon energy that has been boosted incrementally more in comparison to the blue-shift for low excitation power, which is another indication of the presence of subradiant states that emit at higher energies. For high excitation power, the SF state becomes depopulated much faster since more QDs are coupled simultaneously. Then, at long timescales after the initial decay, the percentage of subradiant states becomes dominant, resulting in a blue-shift of the PL emission.

Superfluorescence fit model. SF decay traces as in Fig. 3b cannot be fitted well with mono- or bi-exponential functions because the decay rate is proportional to the number of excited coupled QDs, $\Gamma(N) \propto N$, which also decays over time. Furthermore, the resulting characteristic decay follows neither a stretched-exponential nor a power-law dependence[36] exactly, whereas the PL decay of the uncoupled QDs is well described by a bi-exponential behaviour, where the initial fast decay $\tau_{QD} = 349.8 \pm 0.4$ ps accounts for over 96% the total emitted photons. Nevertheless, we found that the best approximate fit to the SF decay trace as a function of time t is the Kohlrausch stretched-exponential decay model $f(t)/f(0) = \exp[-(\Gamma_{streched}t)^\beta]$, where $f(0)$ is the initial intensity at $t = 0$, $\Gamma_{streched}$ is the average decay time and $\beta \in [0, 1]$ is the stretch parameter, which represents the distribution of decay rates[37]. Using this model to fit the SF decay curve, we obtain an average decay time $\tau_{stretched} = 40.4 \pm 0.5$ ps and a stretch parameter $\beta = 0.457 \pm 0.002$.

At a high excitation density, as shown in Fig. 5b for CsPbBr$_3$ QD superlattices and in Extended Data Fig. 8b for CsPbBr$_2$Cl QD superlattices, we observe oscillations in the decay. To model the SF decay with this characteristic ringing behaviour, we used a decay model consisting of a bi-exponential decay that is multiplied by a damped oscillating term $1 + B\exp(-\gamma_{Damp}t)\cos(\omega t + \phi_0)$, where B is the initial amplitude of the oscillation, ω is its angular frequency, ϕ_0 is its initial phase and γ_{Damp} is its damping constant. Furthermore, for the rising edge of the emitted pulse, which is emitted after build-up time τ_D, we take into account a Gaussian rise term $\exp\{-[(t - \tau_D)/\tau_{rise}]^2\}$, such that the complete fit function is given by[38]:

$$f(t) = \sum_{n=1,2} A_n e^{\frac{\tau_{rise}^2}{4\tau_n^2} - \frac{t - \tau_D}{\tau_n}}$$

$$\times \left\{ \frac{1}{2}[1 + Be^{-\gamma_{Damp}(t - \tau_D)}\cos(\omega(t - \tau_D) + \phi_0)]\left[1 + \mathrm{erf}\left(\frac{t - \tau_D}{\tau_{rise}} - \frac{\tau_{rise}}{2\tau_n}\right)\right]\right\}$$

Here, A_n are the amplitudes of the exponential decay with the corresponding decay time constants, τ_n. Both the fast decay time and the long decay time component (Extended Data Fig. 7d for CsPbBr$_3$ QD superlattices and Extended Data Fig. 9d for CsPbBr$_2$Cl QD superlattices) decrease upon increasing the excitation density, whereas the rise time, $\tau_{rise} = 2.4 \pm 0.3$ ps for CsPbBr$_3$ QD superlattices ($\tau_{rise} = 3.4 \pm 1.0$ ps for CsPbBr$_2$Cl QD superlattices), stays approximately constant (probably clamped by the time resolution of the set-up). In the upper panel of Fig. 5c, we plot the power-dependent effective decay time $\tau_{SF} = (A_1\tau_1 + A_2\tau_2)/(A_1 + A_2)$ for CsPbBr$_3$ QD superlattices, where τ_1, τ_2 are the decay times of the bi-exponential fit and A_1, A_2 the corresponding amplitudes. Assuming that the initial number of coherently coupled QDs is proportional to excitation fluence P_{Exc} with the proportionality constant ζ, the power-dependent effective decay time was fitted with $\tau_{SF}(P_{Exc}) = \tau_{QD}/(\zeta P_{Exc} + 1) + y_0$. Here, a fixed value of $\tau_{QD} = 400$ ps was used, obtained from the time-resolved PL measurements of uncoupled QDs and an additional offset y_0 was inserted to account for effects like the finite time resolution. We obtain good agreement with the expected behaviour ($\tau_{SF} \propto \tau_{QD}/N$ for a value $\zeta_{CsPbBr3} = 0.29 \pm 0.04$ cm^2 µJ^{-1}). In the lower panel of Fig. 5c, we plot τ_D for the CsPbBr$_3$ QD superlattices as a function of the excitation power. In our analysis, the build-up time is composed of the actual delay time due to the SF build-up and a systematic, constant time-offset because the absolute arrival time of the excitation pulse (which has a different wavelength from the emission) at the sample cannot be measured reliably at the required precision from the streak camera data. We observe a decrease in τ_D of about 6 ps when increasing the excitation density by almost 2 orders of magnitude. We have fitted this behaviour for the build-up time τ_D with $\tau_D = y_{offset} + A\ln(\zeta P_{Exc} + 1)/(\zeta P_{Exc} + 1)$ because we assume that $\tau_D \propto \ln(N)/N$ and that the number of excited coupled emitters $N \propto \zeta P_{Exc} + 1$ is proportional to the excitation fluence P_{Exc} with the proportionality constant ζ. Herein, we use a fixed value $\zeta_{CsPbBr3} = 0.29 \pm 0.04$ cm^2 µJ^{-1}, which we obtained from the fit of the effective decay in the upper panel of Fig. 5c, and an amplitude prefactor A. The resulting fit agrees very well with the data. To obtain the absolute time delay, we subtracted the constant offset y_{offset} of the time-delay fit from the time-delay data points. SF occurs when $\sqrt{\tau_{SF}\tau_D} < T_2^*$, where T_2^* is the exciton pure dephasing time, whereas $\sqrt{\tau_{ASE}\tau_D} > T_2^*$ signifies the amplified spontaneous emission (ASE) regime, when τ_{ASE} is the decay time[33]. Considering that the coherence time $T_2 < T_2^*$ extracted from the FWHM of single QDs[11] is of the order of $T_2 = 6.6$ ps, our measurements reveal a fast decay of about 14 ps and a delay time of <1 ps which satisfies the criterion for the appearance of SF.

A similar analysis was performed on CsPbBr$_2$Cl QD superlattices, as shown in Extended Data Fig. 8. In the upper panel of Extended Data Fig. 8c we plot power-dependent effective decay time and fit the data with the same model as described above, using $\tau_{QD} = 250$ ps, and we obtain a value $\zeta_{CsPbBr2Cl} = 0.08 \pm 0.01$ cm^2 µJ^{-1}. The peak intensity of the decay curves as a function of the excitation density is shown in the middle panel of Extended Data Fig. 8c, which increases superlinearly with a power-law dependence with an exponent $\alpha_{CsPbBr2Cl} = 1.3 \pm 0.1$. Also, the build-up time decreases as a function of the excitation density, as displayed in the lower panel of Extended Data Fig. 8c, and fitted the data. Again, we fitted the data using the same formula for τ_D as described above with a fixed value $\zeta_{CsPbBr2Cl} = 0.08 \pm 0.01$ cm^2 µJ^{-1}, and obtained good agreement.
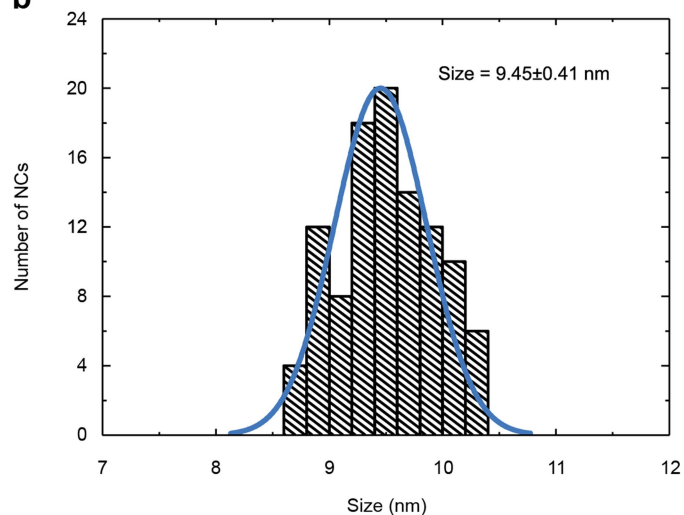
Data availability

The data that support the findings of this study are available from the corresponding authors upon reasonable request.

34. DeVoe, R. G. & Brewer, R. G. Observation of superradiant and subradiant spontaneous emission of two trapped ions. *Phys. Rev. Lett.* **76**, 2049–2052 (1996).
35. Bienaimé, T., Piovella, N. & Kaiser, R. Controlled Dicke subradiance from a large cloud of two-level systems. *Phys. Rev. Lett.* **108**, 123602 (2012).
36. Guerin, W., Rouabah, M. T. & Kaiser, R. Light interacting with atomic ensembles: collective, cooperative and mesoscopic effects. *J. Mod. Opt.* **64**, 895–907 (2017).
37. van Driel, A. F. et al. Statistical analysis of time-resolved emission from ensembles of semiconductor quantum dots: interpretation of exponential decay models. *Phys. Rev. B* **75**, 035329 (2007).
38. Naeem, A. et al. Giant exciton oscillator strength and radiatively limited dephasing in two-dimensional platelets. *Phys. Rev. B* **91**, 121302 (2015).

a

b
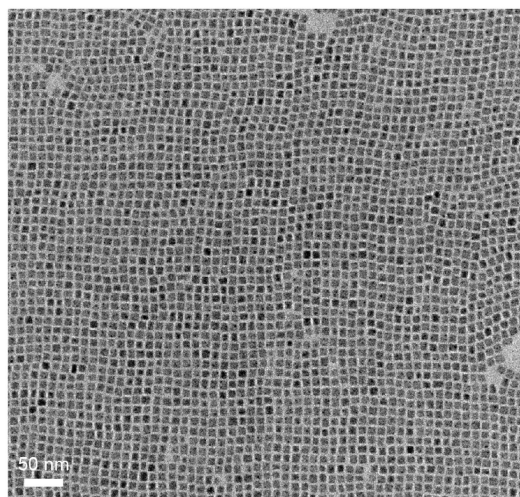
Extended Data Fig. 1 | Quantitative analysis of CsPbBr₃ NC size distribution. a, Low-resolution TEM image of the NC material used to prepare the superlattices. **b**, Histogram of NC sizes (of >100 NCs) as obtained from TEM image analysis. The solid line is a fit with a normal distribution, and the given mean size (9.45 nm) and standard deviation (0.41 nm) are obtained from this fit.
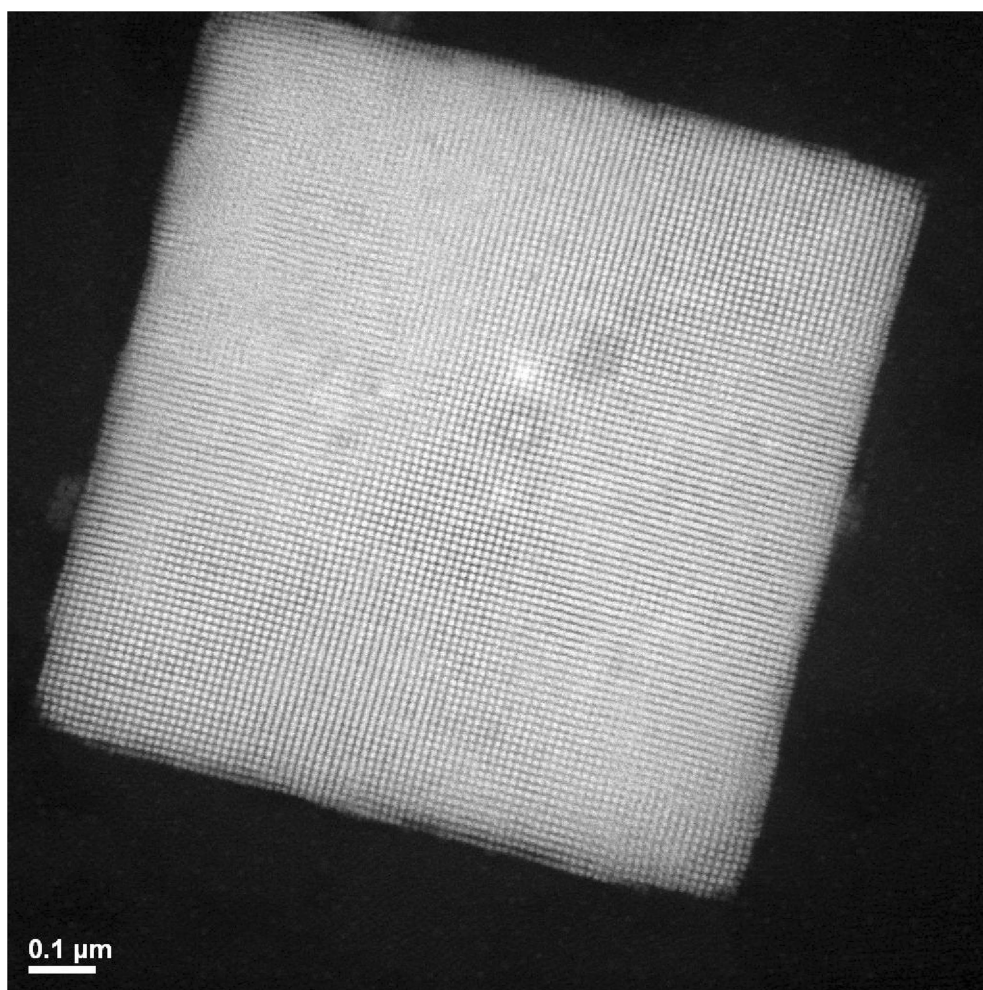
Extended Data Fig. 2 | HAADF-STEM image of a single superlattice of CsPbBr₃ NCs. Individual NCs (bright spots in the image) are well-resolved.
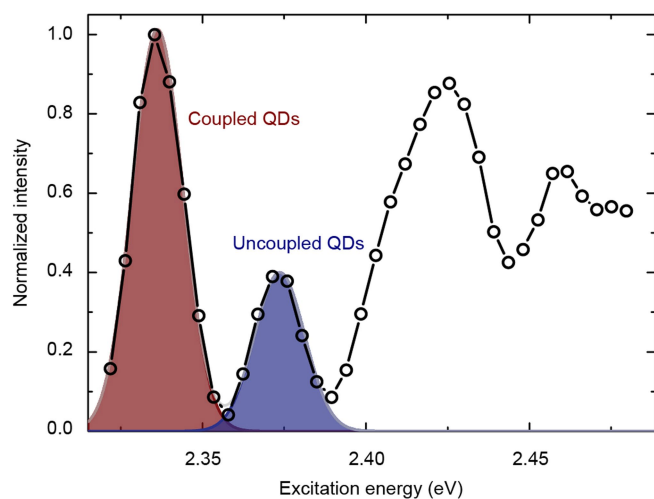
Extended Data Fig. 3 | PL excitation measurement of CsPbBr$_3$ QD superlattices. Using a weak, tunable excitation source, we plot the PL intensity (black circles) obtained at 2.30 eV photon energy as a function of excitation photon energy. The shaded areas are Gaussian peak fits. This PL excitation measurement shows that the coupled QD feature (red) is also present in absorption, in addition to the peak from uncoupled QDs (blue) and energetically higher states.
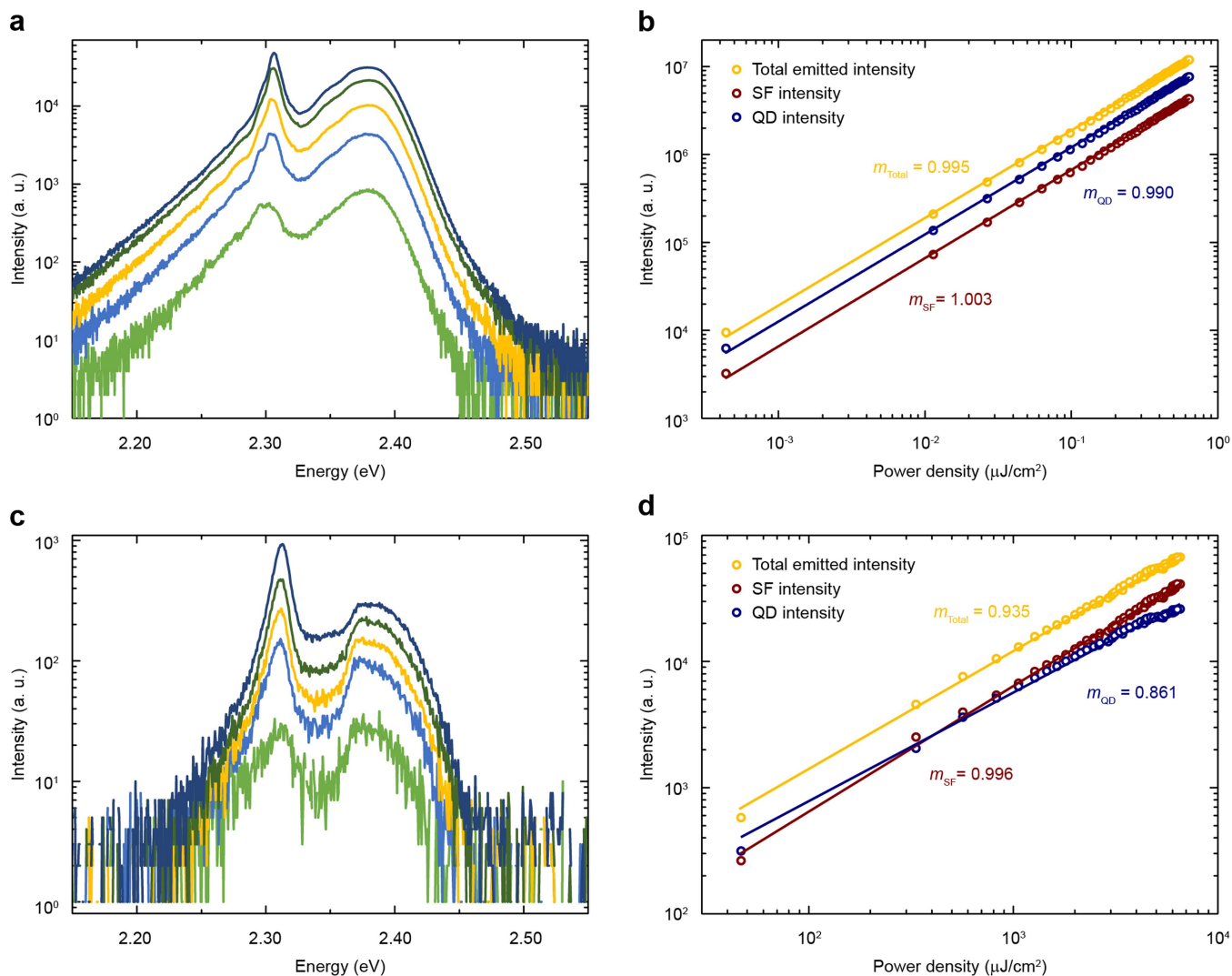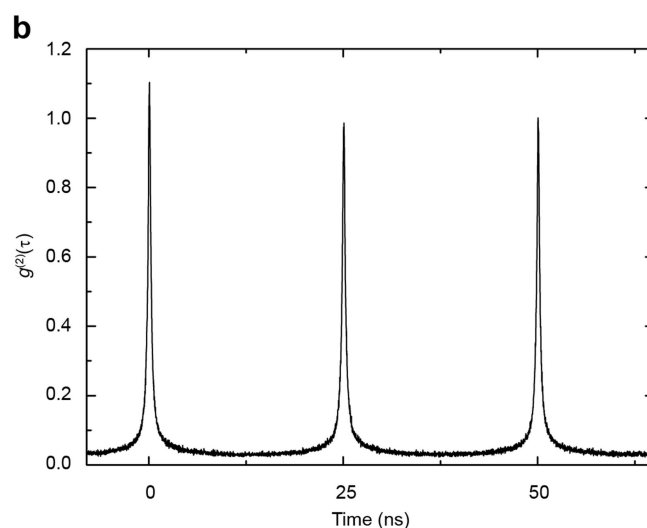
Extended Data Fig. 4 | Power-dependent PL properties of CsPbBr$_3$ QD superlattices. a, Colour-coded PL emission in the low-power excitation regime, shown for increasing excitation fluence (in nJ cm^{-2}) of 10 (light green), 60 (light blue), 150 (yellow) 310 (dark green) and 600 (dark blue). **b**, PL intensity integrated over the spectral emission range of the uncoupled QDs ('QD intensity', blue circles) and coupled QDs ('SF intensity', dark-red circles) in a log–log plot and the total emitted intensity (yellow circles). Fits to the data reveal linear behaviour, as represented by fitted power-law exponents m of approximately 1. **c**, Colour-coded PL emission in the high-power excitation regime, shown for increasing excitation fluence (in μJ cm^{-2}) of 330 (light green), 1,270 (light blue), 2,130 (yellow), 3,470 (dark green) and 6,330 (dark blue). **d**, As **b**, but for the high-power excitation regime. Fits to the data reveal a power-law behaviour with a linear increase for the SF emission, a slightly sublinear increase for the uncoupled QDs and a less sublinear increase for the total emitted intensity.

a

b
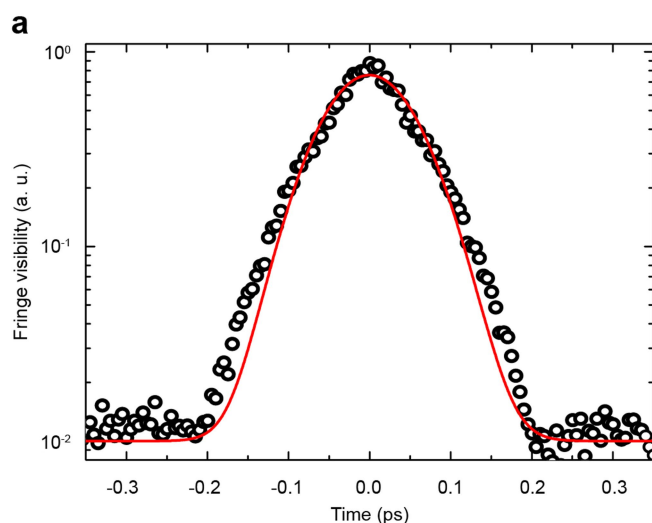
Extended Data Fig. 5 | Gaussian first-order coherence decay and photon bunching in pulsed excitation of CsPbBr$_3$ QD superlattices. a, First-order coherence of the coupled QD emission extracted from the fringe visibility of the interferograms as a function of delay time between the arms of a Michelson interferometer, revealing a mixture of Gaussian (Kubo) and exponential decay (for some of the superlattices). The red solid line is a fit with a mixed Gaussian/exponential model function. **b**, Second-order photon correlation measurement of the coupled QD emission from a single superlattice showing photon bunching at zero delay under pulsed excitation with a 40 MHz repetition rate.
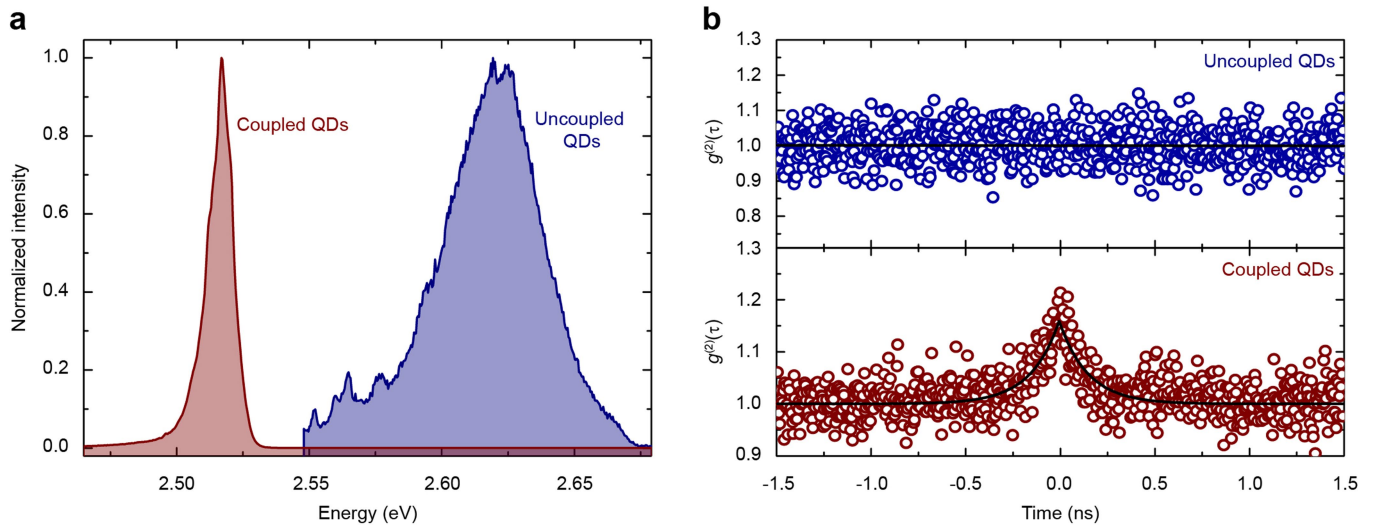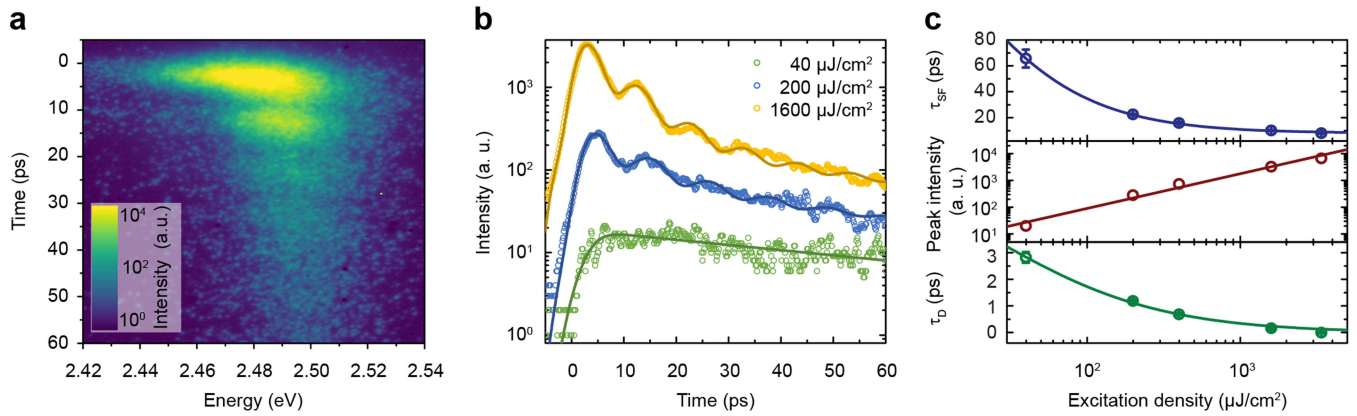
Extended Data Fig. 6 | SF in CsPbBr$_2$Cl QD superlattices. a, Band-pass filtered PL spectra of uncoupled QD emission (blue) and coupled QD emission (red) from CsPbBr$_2$Cl perovskite superlattices. **b**, Second-order photon correlation measurements of uncoupled QD emission (top panel, $g^{(2)}(\tau) = 1$), showing a flat correlation function, and of coupled QD emission (lower panel, $g^{(2)}(0) = 1.15$), showing photon bunching.
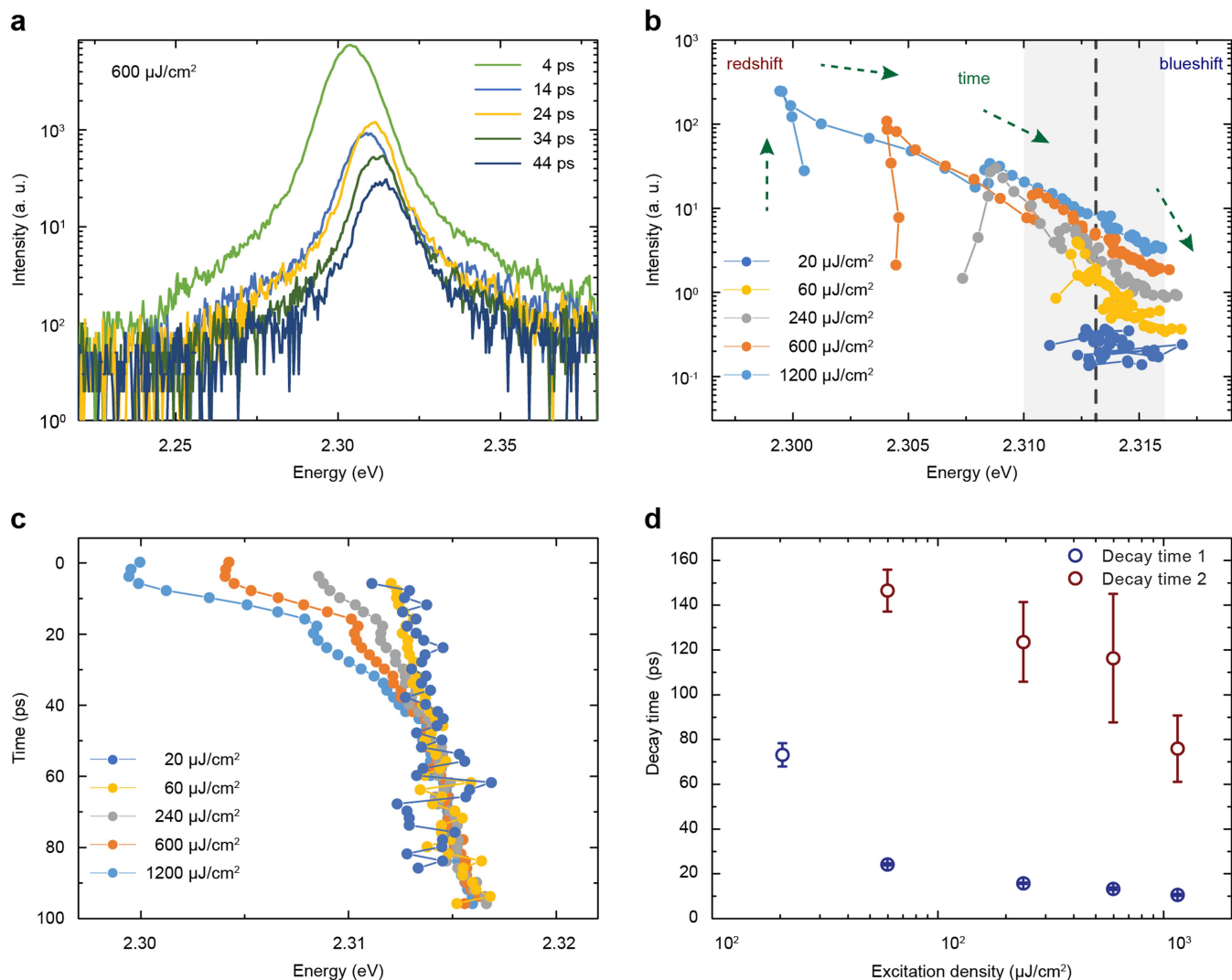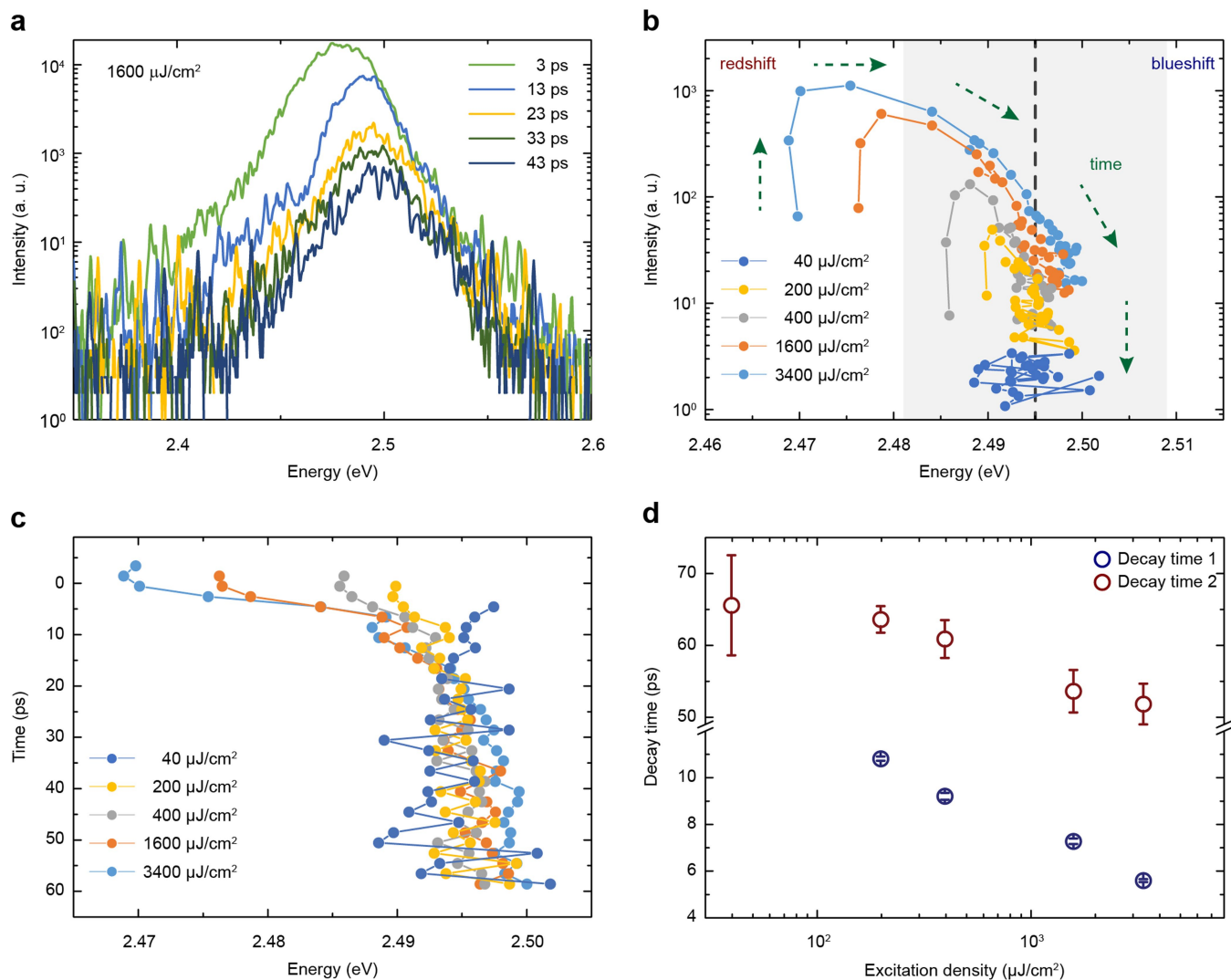
Extended Data Fig. 7 | SF decay and dynamic red-shift of CsPbBr$_3$ QD superlattices. a, PL spectra (integrated over a 2 ps time window) at different time delays on a semi-log scale. **b**, The PL spectra are fitted to a single Gaussian peak function, and the fitted peak amplitude as a function of the emission energy is plotted for various excitation densities (see key). Green arrows indicate the time evolution of the emission peak. The black dashed line denotes the mean energy at the lowest excitation density, and the grey shaded area is the peak's FWHM. **c**, Fitted peak centre energy as a function of time for various excitation densities (see key). **d**, Fast and slow PL decay time components τ_1 and τ_2 of the SF bi-exponential fit model as a function of excitation density on a semi-log plot. The error bars represent the parameters' fit uncertainty.

Extended Data Fig. 8 | Burnham–Chiao ringing behaviour in CsPbBr$_2$Cl QD superlattices. a, Streak camera image of SF dynamics obtained with a high excitation density of 1,600 μJ cm^{-2}. **b**, Extracted time-resolved emission intensity traces for three different excitation powers (see key). Solid lines are best-fits to a model that employs a bi-exponential decay function with damped oscillations. **c**, Top, effective SF decay time (blue circles) as a function of the excitation fluence fitted according to the SF model (solid blue line). Middle, dark-red circles represent the peak SF emission intensity that increases superlinearly with excitation power, corresponding to a power-law dependence with an exponent $\alpha = 1.3 \pm 0.1$ (solid dark-red line). Bottom, the extracted delay time τ_D (green circles) decreases at high excitation power due to the increased interaction among the emitters. The green solid line is the best fit according the model described in the Methods section. The error bars represent the parameters' fit uncertainty.

Extended Data Fig. 9 | SF decay and dynamic red-shift of CsPbBr$_2$Cl QD superlattices. a, PL spectra (integrated over a 2 ps time window) at different time delays on a semi-log scale. **b**, The PL spectra are fitted to a single Gaussian peak function, and the fitted peak amplitude as a function of the emission energy is plotted for various excitation densities (see key). Green arrows indicate the time evolution of the emission peak. The black dashed line denotes the mean energy at the lowest excitation density, and the grey shaded area is the peak's FWHM. **c**, Fitted peak centre energy as a function of time for various excitation densities (see key). **d**, Fast and slow PL decay time components τ_1 and τ_2 of the SF bi-exponential fit model as a function of excitation density. The error bars represent the parameters' fit uncertainty.

a

b
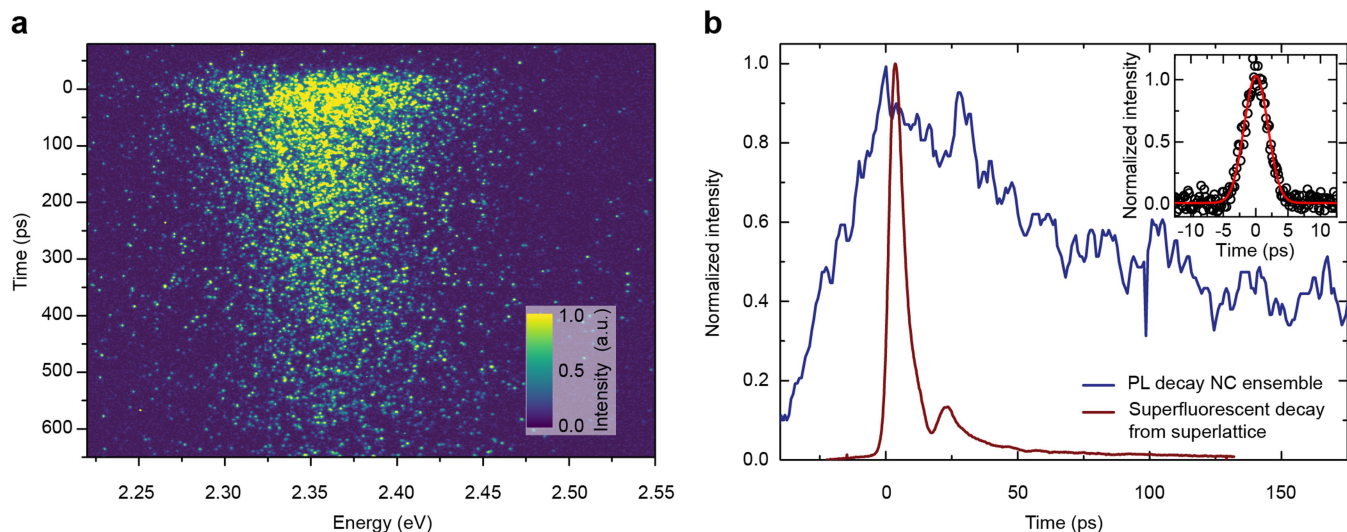
Extended Data Fig. 10 | PL decay from a control sample of diluted CsPbBr₃ QDs. a, Streak camera measurement of a control sample prepared by spin-coating a low concentration of $CsPbBr_3$ QDs dispersed in polystyrene such that no QD coupling is realized. The excitation conditions were comparable to those used in Fig. 5 (an excitation density of 1,600 μJ cm^{-2} was used here). However, the relatively long decay time requires that a longer time range with a lower temporal resolution compared to the measurement in Fig. 5 has to be used on the streak camera. The absence of dynamic red-shift, accelerated decay and ringing proves that the observed SF features cannot be explained by single QD physics but are due to a multi-particle effect. **b**, Time-resolved PL trace (blue) obtained from these streak data. For direct comparison, the equivalent data from a superlattice sample exhibiting SF (Fig. 5b, 1,200 μJ cm^{-2}) is shown (dark red). Inset, instrument response function of the streak camera. Using the same instrument settings as for the measurement on superlattices, the temporal response of the streak camera using scattered light from a 100-fs laser pulse at 400 nm gives a Gaussian-shaped instrument response with a FWHM of 4.3 ps (black circles); a Gaussian fit is shown as the red solid line.